

Density Functional Leveraged Tight-binding Insights into Inorganic Halide Perovskites

Misbah Shaheen and Sheharyar Pervez*

Faculty of Engineering Sciences

Ghulam Ishaq Khan Institute of Engineering Sciences and Technology

(Dated: January 14, 2025)

Compared to first principles studies like DFT (physically accurate, computationally expensive), the TB approach allows the disentanglement of the region of interest, to wit the fermi level. This allows the creation of simplified, highly interpretable models that give chemically grounded insights. In this paper we employ a Wannierized TB approach to tune the bandgap and electronic structure via anion exchange and investigate its impact on the orbital interactives of inorganic lead halide perovskites. Further adjustment of the hopping norm and maximum distance leads to a reduced TB model which regenerates the broad features of the band structure with a fraction of the parameters, thereby making the model simpler and highly interpretable. We observe that due to the asymmetry of the unit cell and the delocalized nature of its orbitals, CsPbBr₂ follows a many-small hopping scheme different in character from the few-big strategy taken by the other perovskites. Finally we leverage the TB model to study the electronic and thermal transport properties of these materials. These insight enable the identification of optimal doping strategies that could enhance thermoelectric performance by improving carrier mobility or optimizing the Seebeck coefficient

I. INTRODUCTION

Functional materials such as inorganic lead halide perovskites (ILHPs) are pivotal to several modern world technology for energy harvesting, energy conversion and waste heat recovery with which we may build a sustainable future [1] [2]. Their flexible structure coupled with interesting physico-chemical properties, such as strong light absorption, bandgap tunability, small exciton binding energy, good carrier mobility and Seebeck coefficient, and ultralow thermal conductivity across a range of compositions and phases; makes them promising candidates for photovoltaic and thermoelectric applications. [3]

Both the crystal structure and the bandgap heavily dependent on the anion composition. Since the soft crystal structure of these materials facilitates diffusion of the halide ions through the crystal lattice, anion exchange driven dynamical disorder can be used to tune the bandgap, improve carrier transport, and consequently enhance thermal and optical profiles [4]. The Goldschmidt tolerance factor t and the octahedral factor (μ), which measure geometric stability, are expected to lie between 0.8 – 1.1 and 0.44 – 0.9, respectively for a stable perovskite structure [5]. The exchange of the A-site and/or X-site restores the tolerance factor closer to 1, thus stabilizing the cubic structure at room temperature [6] [7].

To solve for the electronic structure, in order to predict the physical and chemical properties, we have at our disposal first principles methods like DFT, which try to solve approximations of the many-body Schrodinger equation. Though more accurate, these are also computationally expensive. Tight-binding models are a popular, computationally less intensive alternative where a

good model Hamiltonian is one which captures key features of the region of interest with minimal requirements.

In this study we tune the cubic phase ILHPs bandgap via anion exchange and examine the resulting impact on electronic and thermoelectric properties using a synergetic density functional theory (DFT) and tight binding (TB) approach. The TB approach allows us to create a model that is chemically grounded and computationally simple. Further examination leads us to a reduced TB (redTB) model which is readily interpretable. The redTB model highlights the key elements of the ILHP Hamiltonian. Finally we categorize the materials according to a many-small vs. few-big (MSFB) scheme based on the distribution of hopping spectrum.

The rest of the paper is organized as follows. First we present the background on DFT, the tight-binding method, and transport properties. We then detail our methodology and finally the interpretation of results where we present the reduced TB method and discuss the thermoelectric profiles.

II. PRELIMINARIES

A. Density Functional Theory (DFT) and Tight Binding (TB)

Conventional Kohn-Sham DFT framework uses Bloch states $\psi_{nk}(\mathbf{r})$ to solve the KS equations for a fictitious system of non-interacting particles instead of the many body Schrodinger equation of the fully interacting Hamiltonian. The eigenstates extend over the Brillouin zone, and are required to be orthogonal, which makes the computational complexity grow cubically with system size.

Subjecting the DFT deduced Bloch orbitals $\psi_{n,k}(r)$ to a unitary transformation matrix \mathcal{U} , one can generate localized orthonormal orbitals, called Wannier functions (WFs) $w_n(\mathbf{r} - \mathbf{R})$, identified by the band index n , and

* sheharyar@giki.edu.pk

the unit cell vector \mathbf{R} [8].

$$|w_n(\mathbf{r}-\mathbf{R})\rangle = \frac{V}{(2\pi)^3} \int_{BZ} dk \sum_{m=1}^N e^{i\cdot k\cdot R} \mathcal{U}_{mn}(k) |\psi_{n,k}\rangle \quad (1)$$

where $\mathcal{U}_{mn}(k)$ are the elements of the unitary transformation matrix at a specific k . The degree of localization is determined by the spread functional Ω as:

$$\Omega = \sum_{n=1}^N (\langle r^2 \rangle_n - \langle r \rangle_n^2) \quad (2)$$

Minimizing this functional yields Maximally Localized Wannier functions (MLWFs) [9]. MLWFs allow the problem to scale more linearly, and aid in the construction of model Hamiltonians such as those in the TB approximation [10]:

$$H(k) = \sum_i E_i(\mathbf{R}_a) c_i^\dagger c_i + \sum_{(i,j)} t_{ij}(\mathbf{R}_a) c_i^\dagger c_j + h.c. \quad (3)$$

Here H is the TB Hamiltonian, $E_i(R_a)$ is the on-site energy, $t_{ij}(R_a)$ are hopping parameters (between i -th orbital in home unit cell at $R = 0$ and j -th orbital in a unit cell at \mathbf{R}), c_i^\dagger and c_i are creation and annihilation operators, respectively and \mathbf{R}_a are atomic positions.

Semi-empirical TB is an intuitive and computationally efficient approach towards evaluating crystal systems, in which the hopping parameters are often obtained from the overlap between the relevant atomic orbitals [11]. Accuracy is sacrificed for speed, simplicity, and interpretability. This is in direct contrast to first principles calculations. Wannierized TB models seek a balance, leveraging the simplicity of empirical methods with the accuracy from ab initio calculations. They are important in studying semiclassical theory of electron dynamics that has been implemented in this article. They can yield simplified and highly interpretable insights by significantly reducing the degrees of freedom and providing flexibility in parametrizing the Hamiltonian.

B. Transport Properties

Electronic properties of perovskites can be determined through their band structure, obtained by solving the many body Schrodinger equation, and the density of states (DOS) given by:

$$g(E) = \frac{1}{2\pi^2} \left(\frac{2m^*E}{h^2} \right)^{3/2} E^{1/2} \quad (4)$$

where, E is the dispersion relation ($h^2k^2/2m^*$).

Thermoelectric transport properties are quantified by electrical (σ) and thermal (κ) conductivity, and Seebeck

coefficient (S) at a specific temperature. Boltzmann transport equation provide the semiclassical treatment to study the transport properties of materials with complex band structures [12].

In semiclassical transport theory framework, the expressions for σ , S and κ tensors are:

$$\sigma = e^2 \int \Sigma_E(E) \frac{-\partial f}{\partial E} dE \quad (5)$$

$$S = \frac{e}{T} \int \Sigma_E(E - E_F) \frac{-\partial f}{\partial E} dE \quad (6)$$

$$\kappa_{el} = \frac{1}{T} \int \Sigma_E(E - E_F)^2 \frac{-\partial f}{\partial E} - TS^2\sigma \quad (7)$$

where, E_F is the fermi energy, f is the Fermi-Dirac distribution, and Σ_E is the transport distribution function (TDF), a tensor sum over v_i , the i -th component of band velocity, and the relaxation time τ :

$$\Sigma_{E_{ij}}(E) = \frac{1}{V} \sum_{n,k} v_i(n,k) v_j(n,k) \tau(n,k) \delta(E - E_{n,k}) \quad (8)$$

Here, V is the volume of system, n is the band index at crystal momentum, k .

These parameters then collectively control the Figure of Merit (ZT), the principal metric used to judge thermoelectric materials:

$$ZT = \frac{\sigma S^2 T}{\kappa} \quad (9)$$

High performing thermoelectric materials (high ZT) should have high σ and S , and low κ .

III. METHODOLOGY

In order to investigate the inorganic lead halide perovskites with partial and complete anion exchange for their structural, electronic and thermoelectric properties, we followed the four step workflow presented in Fig. 1.

Structure Generation: The four crystalline perovskite structures, CsPbBr₃ CsPbBr₂I CsPbBrI₂ and CsPbI₃ were generated using Vesta [13] and relaxed using Quantum Espresso. Table I shows the geometrical details of perovskite structures: Goldschmidt tolerance factor (t), octahedral factor (μ), unit cell volume, and electronegativity. The structures are cubic and pseudocubic with $Pm\bar{3}m$ space group. The parameters t and μ , were calculated using the equations (10) and (11):

$$t = \frac{r_A + r_X}{\sqrt{2}(r_B + r_X)} \quad (10)$$

TABLE I: Structural properties of perovskites

Material	Goldschmidt tolerance	Octahedral factor	Unit cell Volume ($a.u.$) ³	Electronegativity
CsPbBr ₃	0.862	0.61	1455	4.55
CsPbBr ₂ I	0.858	0.58	1553	4.47
CsPbBrI ₂	0.855	0.56	1653	4.34
CsPbI ₃	0.851	0.54	1623	4.28

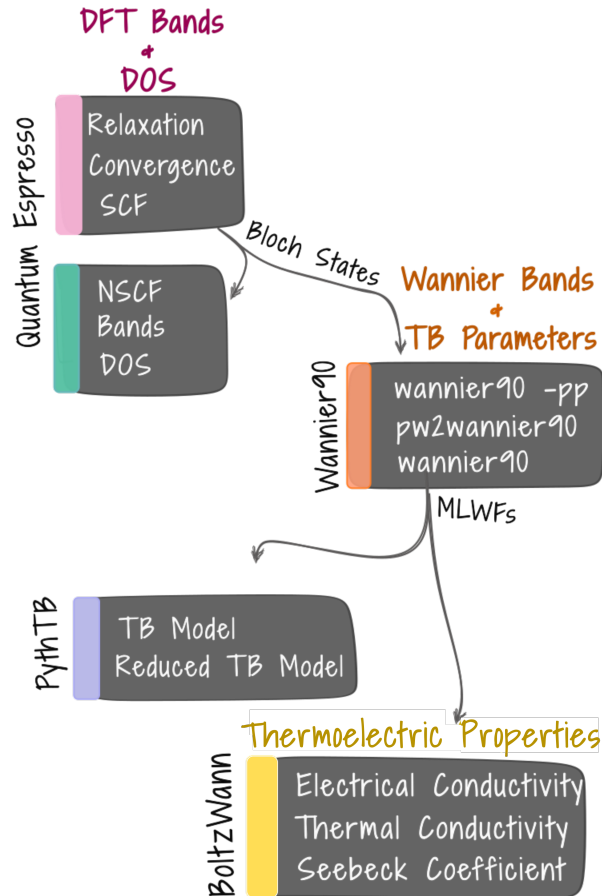


FIG. 1: Workflow showing the detailed steps followed for computations. The Bloch states computed using DFT were fed for wannierization. The MLWFs thus generated were utilized for the TB models and thermoelectric evaluation.

$$\mu = \frac{r_B}{r_X} \quad (11)$$

where r_A , r_B and r_X are the Shannon radii of the Cs, Pb and X=Br and I, respectively in the perovskite structure.

DFT Calculations: DFT calculations were performed using the Generalized Gradient Approximation (GGA) Perdew-Burke-Ernzerhof (PBE) exchange-correlation (XC) with Quantum Espresso (QE), version 7.2 [14] [15] to obtain the bandstructure and density of

states (DOS). Variable cell relaxation was performed for each structure prior to calculations. Convergence tests were carried out for `ecutwfc`, `ecutrho`, and Monkhorst-Pack k-points mesh. Further details of convergence parameters are given in Table S1.

Wannierization and Tight-Binding: Parametrized tight binding model was created using Wannier90 (W90) [16] and `pythtb` [17]. The `pythtb` code was modified to generate TB as well as `redTB` model. A twelve member basis set was selected for p orbitals of Pb and halogen atoms present in perovskite structures.

`Pythtb` code was implemented to extract the on-site energies and hopping parameters for both TB and `RedTB` models. TB model utilizes all the contributions however `RedTB` model require bare minimum threshold of nearest neighbors and hopping norm.

Thermoelectric Properties: Finally, the developed `tb` model has been applied to study thermoelectric properties of perovskites through utilizing the knowledge of transport phenomenon implemented through Boltzmann transport equation. Calculations were performed using Boltzmann module of `postw90` by varying the μ from in the vicinity of fermi energy (as bands only in this region with width of $k_B T$ around fermi energy are relevant). Figure of merit ZT (equation (9)) is calculated after obtaining the electrical conductivity (σ), Seebeck coefficient (S), thermal conductivity ($\kappa = \kappa_{\text{electronic}} + \kappa_{\text{Lattice}}$) at different temperatures T .

IV. RESULTS AND DISCUSSION

A. DFT Results

The DFT generated band structure along the selected k-path and the corresponding density of states (DOS) for the materials, with contributions from the lead and halogen s and p orbitals, are shown in Fig. 2, with all four systems having direct bandgaps at R. As is usual for perovskites, Cs orbitals play more of a stabilizing role and contribute relatively little to the bands or the band gap. Their DOS contributions reside in the higher end of the conduction band, away from the region of interest, and are not shown.

The valence bands comprise principally the nine halogen centered p orbitals with some hybridization induced contribution from the Pb-s and Pb-p orbitals whereas the Pb-p and X-p orbitals feature prominently in the lower half of the conduction band. CsPbBr₃ and CsPbI₃

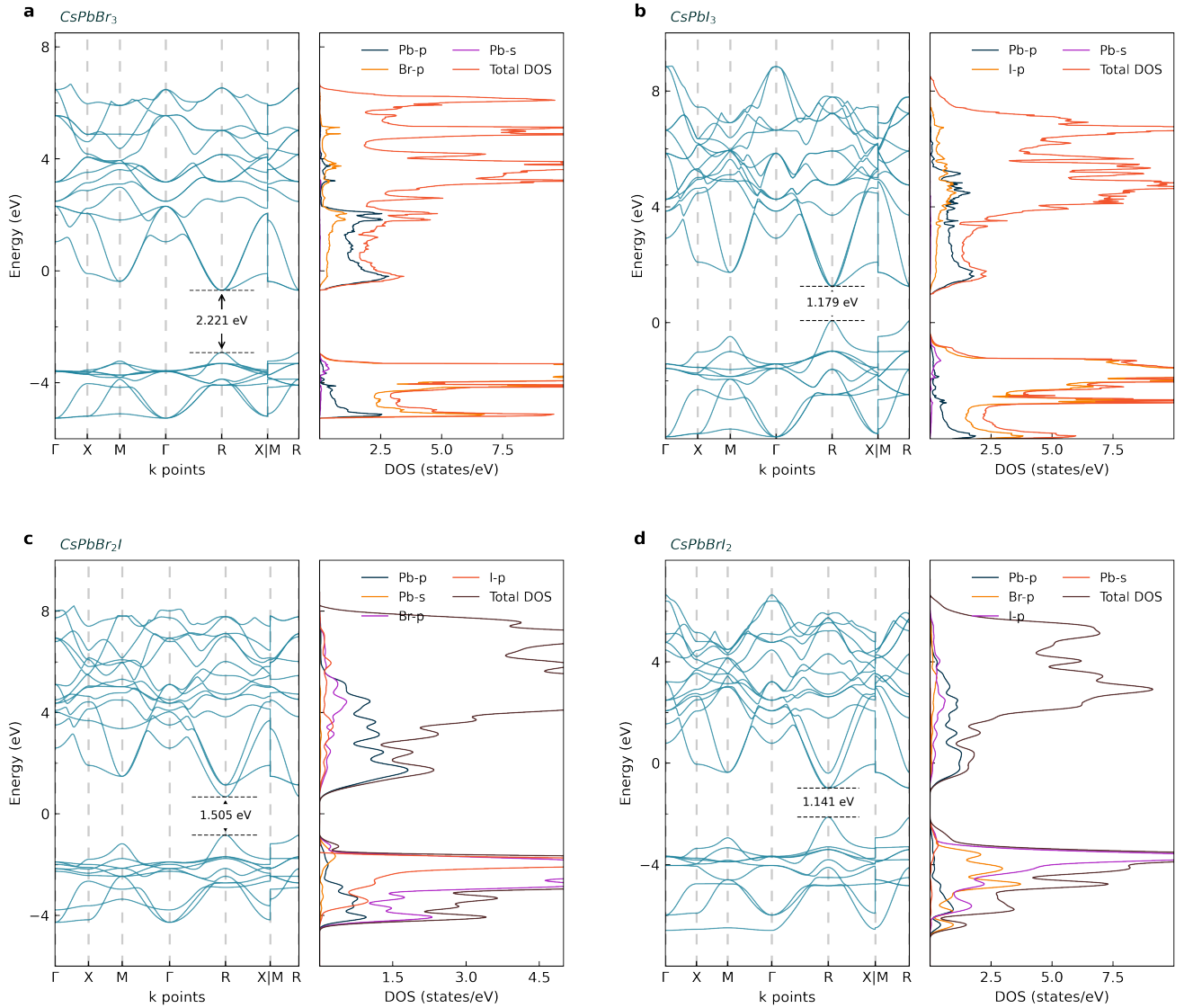


FIG. 2: Band structure along high symmetry points and density of states for perovskites obtained from DFT calculations. Anion exchange tuned the bandgaps resulting in maximum bandgap for CsPbBr₃ and minimum bandgap for CsPbBr₂I .

show a high degree of degeneracy which is lifted as we move to their less symmetric anion exchanged counterparts, CsPbBr₂I and CsPbBrI₂. In addition to its significantly smaller bandgap, CsPbBrI₂ bands also exhibit dense packing and small dispersion attributable to the slight shifting of halogen atom with reference to Pb atom [18].

Thermoelectric bandgaps need to be large enough to isolate n-type and p-type carriers, but small enough to assist mobility. The 2.221 eV bandgap shown by CsPbBr₃ can be tuned by keeping the A and B cations constant while swapping the X anions, thus giving us bandgaps in the order CsPbBr₃ > CsPbBr₂I > CsPbI₃ > CsPbBrI₂.

Carrying out partial substitution on the unary halogen CsPbBr₃, and CsPbI₃, to yield the binary halogens

CsPbBr₂I and CsPbBrI₂ results in a loss of symmetry, as evidenced by the lattice parameters, Goldschmidt tolerance t and octahedral tilt μ in Table I. The reduced symmetry increases the overlap between orbitals which narrows the bandgap. Going from CsPbBr₃ to CsPbI₃, brings the valence band from 4p to 5p. The decreased electronegativity, and hence binding energy and ionization potential, also lead to an increase in the unit cell volume. The reduced the orbital overlap between the metal and halogen atoms, thus reduces the bandgap by influencing the edge states of the valence and conduction bands. Fig. 3 shows this inverse relationship between bandgap and the unit cell volume. A slight increase takes place as we restore symmetry in going from CsPbBrI₂ to CsPbI₃ because the volume is optimized to a cubic

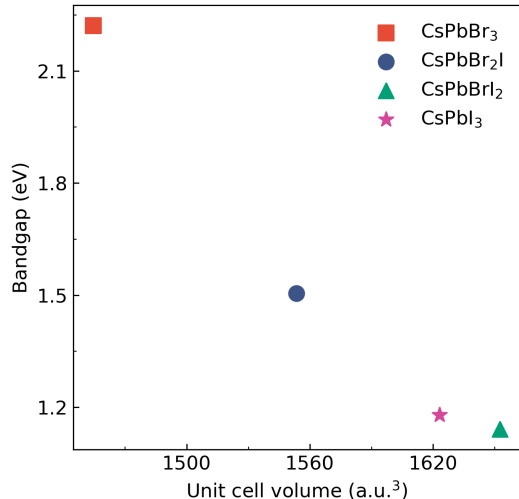


FIG. 3: Relationship between cell volume and bandgap shows a downward trend because of the reduced orbital overlap.

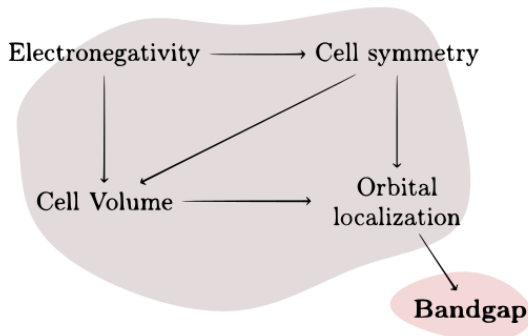


FIG. 4: Relation between different structural and chemical properties that influence the bandgap of perovskites

minima. The interplay between cell geometry and electronegativity effected through anion exchange ultimately influences the bandgap via the orbital localization and is conceptualized in Fig. 4. The combined effect of all these competing factors is mediated through the shifting bandgap [19].

B. Wannierization and Tight-binding

The band structures when regenerated post Wannierization follow the DFT generated profile quite closely S1. The Wannier orbitals for CsPbBr₃ thus obtained are shown in in Fig. 5. See Fig. S2– S4 for the remaining materials. The Wannierization employed a 12 orbital basis set: the p_x , p_y , and p_z orbitals for one Pb

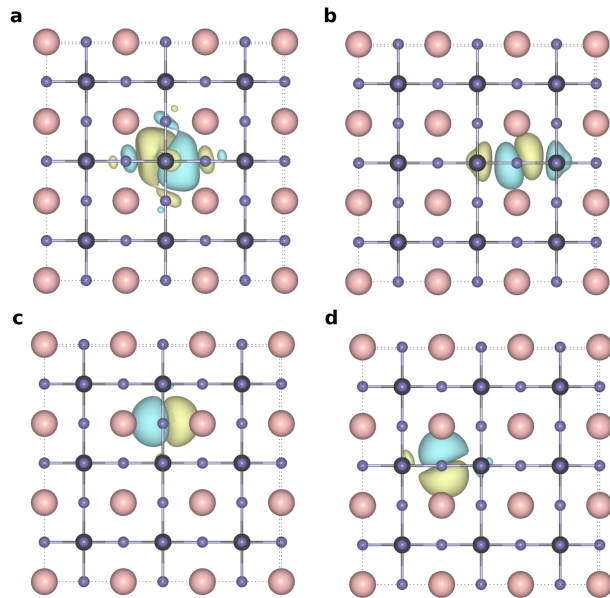


FIG. 5: Heat maps showing the tight binding scheme with twelve wannier orbitals. Diagonal entries are on-site energies and off-diagonal values are hopping parameters with spreads of wannier orbitals are displayed on top of the grid (Pb: dark green, Br: medium green, I: light green). The color bar shows the extent of overlap with green being greater. CsPbBrI₂ shows a uniform field, where as CsPbI₃ is more selective.

and three X atoms, with one p orbital on each halogen atom directed along the Pb-X-Pb axis.

Wannierization allows the construction of a tight binding (TB) model. The $3 \times 3 \times 3$ supercell generated models are shown as heat maps along with the spread of Wannier functions in Fig. 6. The log of on-site energies are placed along the diagonal and hopping strengths off it. As a sanity check it can be seen that Pb-Pb hoppings, say for CsPbBr₃ are small due to their orthogonal nature but large between Pb and Br for row 3 because of its orientation along the line Pb-X-Pb.

It will be noted that the heat maps are more uniform in the case of CsPbBr₂I and CsPbBrI₂.

By comparison, the more delocalized CsPbBr₂I contains stronger hoppings, from farther away. Put another way, the ionic behavior in CsPbBrI₂ is thus less selective and more gregarious than say CsPbI₃. Moreover, the orbitals (coded as dark green for Pb, medium green for Br, and light green for I) already considerably spread out for the Pb centered p orbitals relative to the X, delocalize further for the iodine based materials, for example CsPbBrI₂ versus CsPbBr₃. This is again a manifestation of the loss of symmetry. In other words, the push towards delocalization through increased cell volume and lower electronegativity is countered to some extent through the loss of symmetry. This leads us to the scheme in Fig. 4 where the unit cell volume and direction of orbitals both

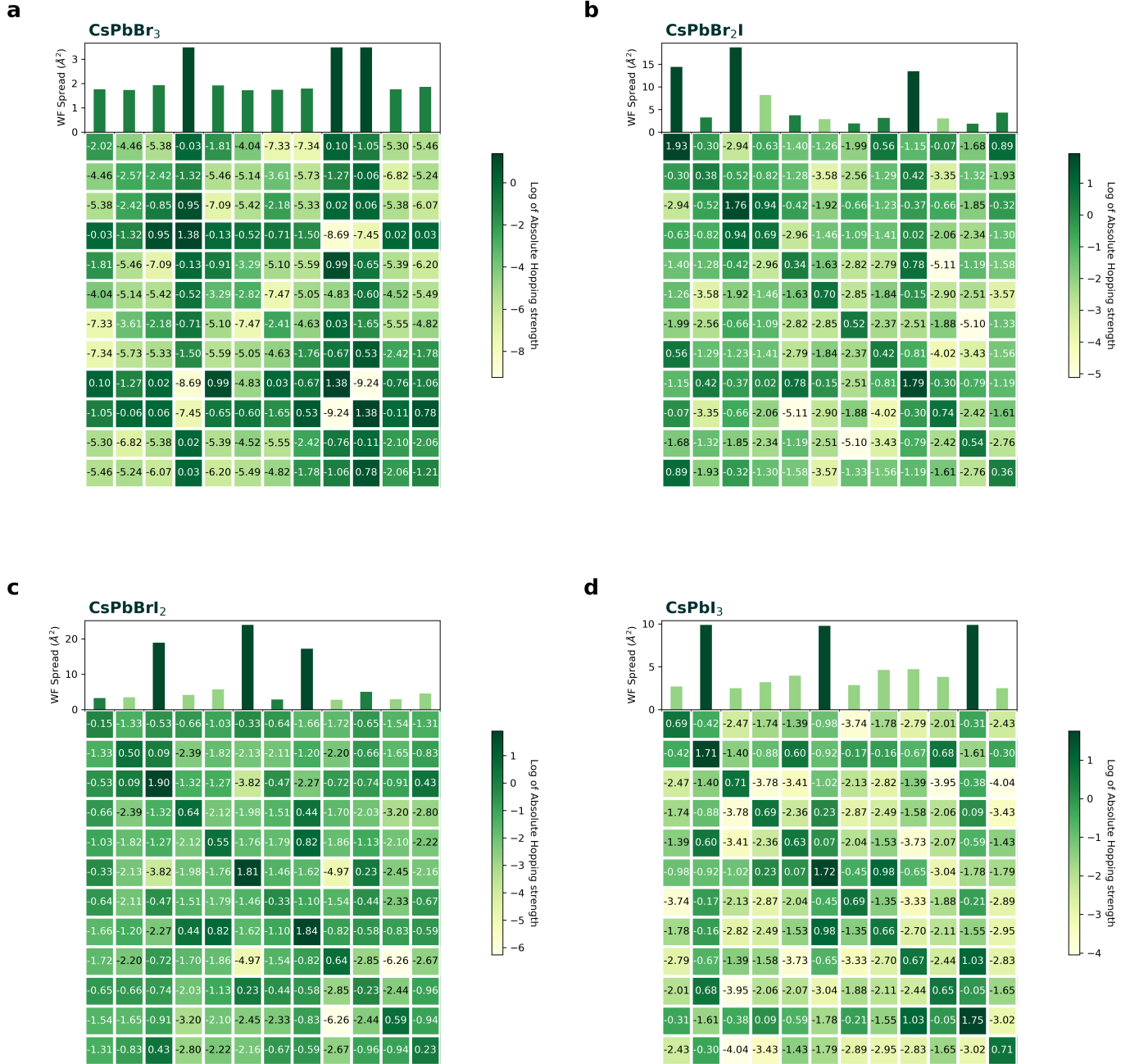


FIG. 6: Heat maps showing the tight binding scheme with twelve wannier orbitals. Diagonal entries are on-site energies and off-diagonal values are hopping parameters with spreads of wannier orbitals are displayed on top of the grid (Pb: dark green, Br: medium green, I: light green). The color bar shows the extent of overlap with green being greater. CsPbBrI₂ shows a uniform field, whereas CsPbI₃ is more selective.

influence the orbital localization and hence the bandgap. In the TB paradigm we discuss below, this would be effected via the changes in the hopping weights.

Fig. 7a shows a randomized 10,000 point sample of the hoppings that lie within 1.5 times the average lattice

length. CsPbBr₃ with its localized orbitals and smaller unit cell has a wider spectrum of hoppings, both weak and strong, within the specified region. Almost similar is the case of CsPbI₃ but the delocalized orbitals of CsPbBr₂I and especially CsPbBrI₂ make more dispersed

hopping spectrum over pointing towards the more contributions of weak strength.

The complete TB model contains redundant information. A leaner model, one that uses fewest hops, can be created by adjusting the maximum distance and minimum hopping thresholds. The CsPbBr₃ Wannier bands under two thresholds are shown in 7b. The orange curves have a minimum hopping strength of 0.001 eV and no maximum distance cutoff apart from the dimension of the supercell. On the other hand, with a hopping cutoff of 0.06 eV and a maximum distance cutoff of 1.5 times lattice vector, the blue curve can recover the key feature of the bands profile with only a fraction of terms (roughly 0.1%). This leads to the reduced TB (RedTB) scheme of fig. 7c which is considerably sparser and shows the most essential hops. Table II contains the threshold value of hopping norm and corresponding number of hopping parameters required to recover the bands. redTB maps along with the recovered bands with minimum hopping norms for other three perovskites are added in figures S5– S7. As can be seen in Supplementary figure S6, the redTB map for CsPbBrI₂ is unique in maintaining a uniform profile. A look at the hop distribution in the reduced framework (Fig. 7d) gives insight as to why this is so. CsPbBr₃ and CsPbI₃ with their confined orbitals, follow a ‘few-strong’ scheme: a few hops of greater strength are sufficient to capture the essential details of the band structure. The spectrum of CsPbBrI₂ is unique in following a ‘many-weak’ scheme: many hops, though of weaker strength are needed to recreate the bands profile.

The ‘social’ networks of Fig. 8, expressing the reduced scheme of CsPbBr₃ and CsPbBrI₂, show the contrast between the reserved nature of the former with the gregarious nature of the latter: i.e. the few-strong strategy for CsPbBr₃ versus the many-weak one for CsPbBrI₂.

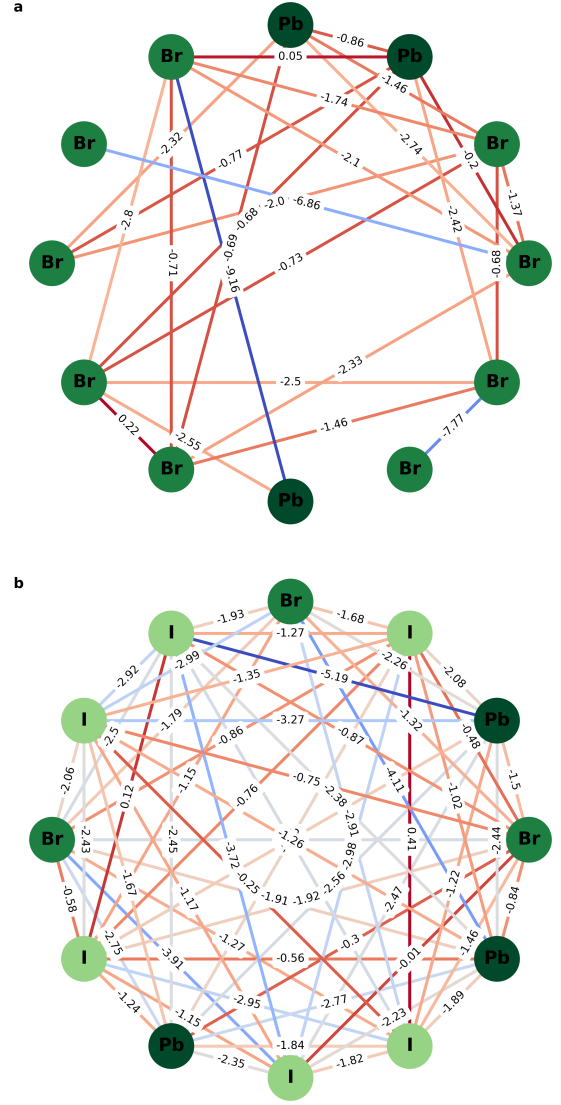


FIG. 8: The redTB Hamiltonians expressed as network graphs contrasts the sociable nature of CsPbBrI₂ orbitals (*bottom*) with the reserved behavior of CsPbBr₃ (*top*). Connections are colored from red to blue in decreasing values of the log of hopping parameters which are shown on each edge.

C. Thermoelectric Properties

The semiclassical Boltzmann Transport equation describes the electrical transport properties of bulk materials under the influence of an electric field \mathbf{E} and temperature gradient ∇T . To examine the effect of anion exchange on the thermoelectric properties, the transport properties in relaxation time approximation were evaluated via semi-classical formalism using MLWF basis

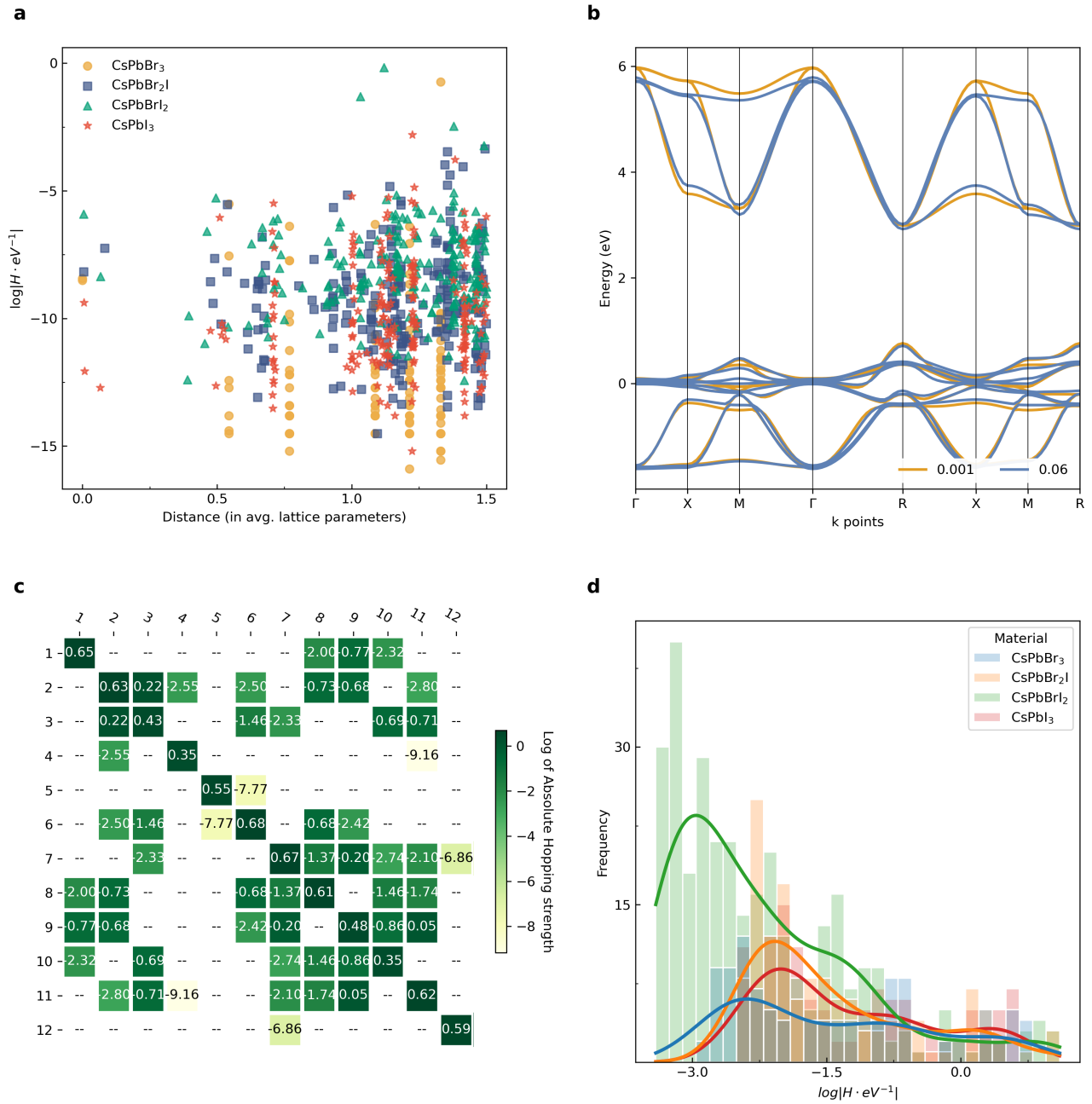


FIG. 7: (a) Hopping contributions of all perovskites in terms of distance from home cell. The contributions are localized on specific values of distance for symmetric structures CsPbBr₃ and CsPbI₃, and are scattered over the plot for anion exchanged structures CsPbBr₂I and CsPbBr₂. (b) Wannier bands recovered for CsPbBr₃ in reduced tight binding scheme with minimum hopping norm of 0.06. (c) Heat map for CsPbBr₃ showing the minimum contributions in reduced tight binding scheme that can recover the band structure. (d) Density plot showing the hopping distributions for perovskites.

within the presented TB model [20].

Fig. 9(a-d) show the computed thermoelectric properties σ , κ , S , and ZT vs. the chemical potential (μ) with each curve shifted by its corresponding Fermi energy so that the the axis zero corresponds to the charge

neutrality point. As mentioned, a material with excellent electrical conductivity, large Seebeck coefficient, and low thermal conductivity would correspond to a high figure of merit. Materials with values ZT close to unity in the vicinity of the Fermi level, as we have here, would

TABLE II: The number of parameters in the redTB formalism with the threshold, mean, and standard deviation of log of hopping strengths in eV

Material	Num. of parameters	Min. threshold	Mean	Std dev
CsPbBr ₃	104	-2.81	-1.422	1.115
CsPbBr ₂ I	136	-2.41	-1.433	0.928
CsPbBrI ₂	316	-3.35	-2.218	1.036
CsPbI ₃	120	-2.47	-1.276	0.955

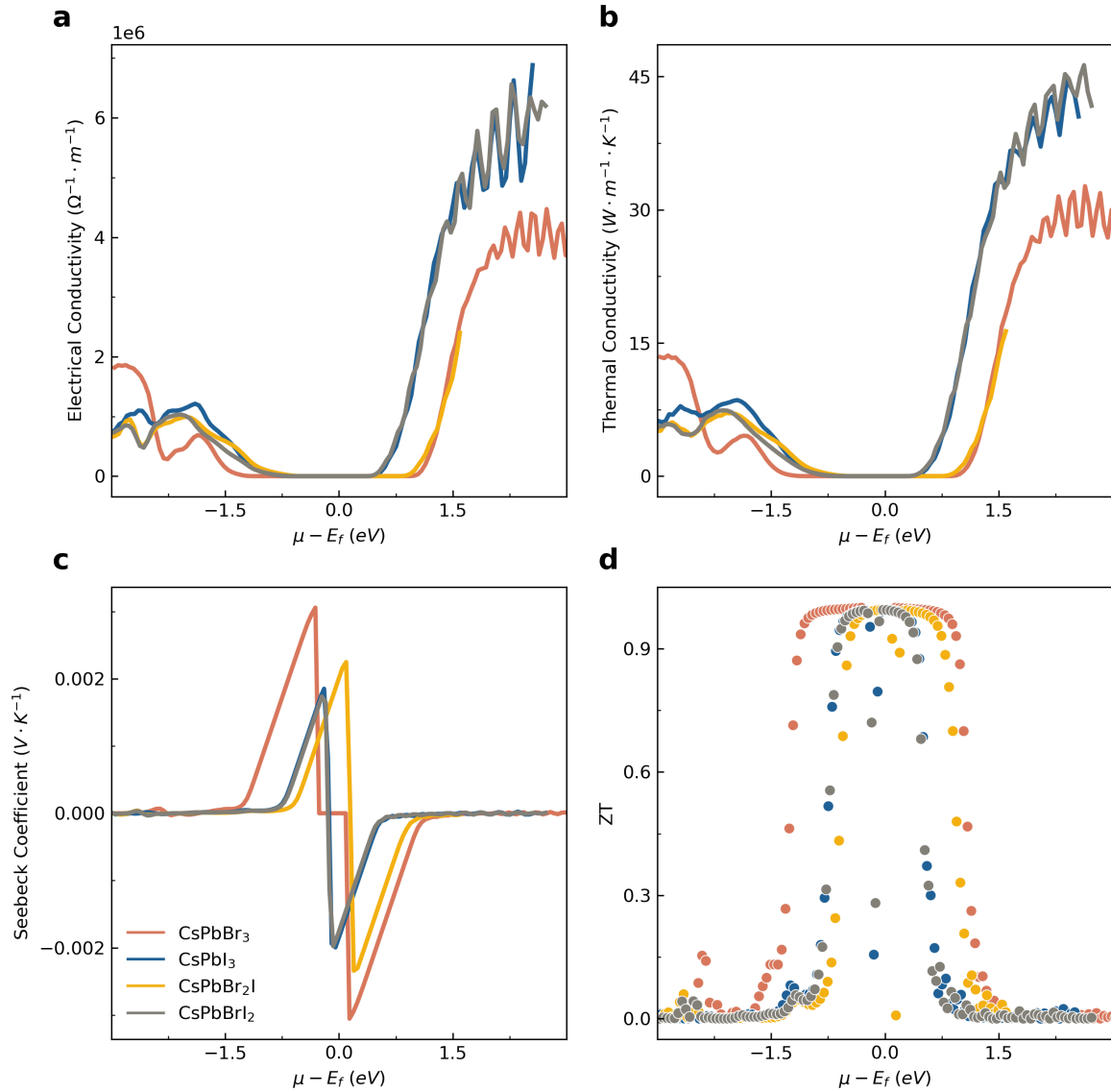


FIG. 9: Thermoelectric properties of perovskites showing the (a) Electrical conductivity, (b) Thermal conductivity, (c) Seebeck coefficient and (d) Figure of merit (ZT).

be regarded as good thermoelectric materials. Positive (negative) values of the Seebeck coefficient correspond to p-type (n-type) behavior in which holes (electrons) would be the charge carriers. The coefficient, as maybe seen in 9(c), is higher close to the charge neutrality point for all four cases with the broadest profile being displayed by CsPbBr₃. The larger bandgaps of CsPbBr₃ and CsPbBr₂I hinders transport and results in lower conductivities. Within the linear region of the plot the electrical and thermal conductivities of CsPbI₃ and CsPbBrI₂ are almost three times larger, although these two materials also achieve higher values of the Seebeck coefficient. The thermal and conductivities follow a similar profile with a constant ratio. Hence the figure of merit ZT is conditioned predominantly by the Seebeck coefficient. Hence the broad profile of CsPbBr₃ albeit with a low Seebeck coefficient around the Fermi level is reflected in the 9(d) Moreover, the asymmetric nature of the conductivity curves, with higher values for $\mu > E_f$, indicates that the materials is more suited to electron doping than hole.

V. CONCLUSION

Anion exchange allows the tuning of the bandgap to counter the instability of the phases. This begs the

question: what is it that happens at the molecular orbital level. Our TB and redTB models generated using MLWFs shed some light on this. The TB profile of CsPbBrI₂, which coincidentally has the smallest bandgap, is qualitatively and quantitatively different from the other three in the vicinity of the Fermi level, as evidenced by the lack of variation in its TB Hamiltonian. Closer examination via the redTB model and network analysis shows that while the remaining three have a core set of important relationships, the delocalized nature of CsPbBrI₂ manifests itself in a reduced matrix that shows many hops that are weaker in strength.

ACKNOWLEDGMENTS

The authors gratefully acknowledge the support of GIK Institute of Engineering Sciences and Technology for providing essential computational facilities for this research. Special appreciation is extended to Dr. Adeel Pervez for providing technical support on various issues.

-
- [1] C. He and X. Liu, The rise of halide perovskite semiconductors, *Light: Science & Applications* **12**, 15 (2023).
- [2] J. Tian, Q. Xue, Q. Yao, N. Li, C. J. Brabec, and H.-L. Yip, Inorganic halide perovskite solar cells: Progress and challenges, *Advanced Energy Materials* **10**, 2000183 (2020), <https://onlinelibrary.wiley.com/doi/pdf/10.1002/aenm.202000183>(2018).
- [3] M. A. Haque, S. Kee, D. R. Villalva, W.-L. Ong, and D. Baran, Halide perovskites: Thermal transport and prospects for thermoelectricity, *Advanced Science* **7**, 1903389 (2020).
- [4] J. A. Steele, M. Lai, Y. Zhang, Z. Lin, J. Hofkens, M. B. J. Roeyfaers, and P. Yang, Phase Transitions and Anion Exchange in All-Inorganic Halide Perovskites, *Accounts of Materials Research* **1**, 3 (2020), publisher: American Chemical Society.
- [5] V. M. Goldschmidt, Die Gesetze der Krystallochemie, *Naturwissenschaften* **14**, 477 (1926).
- [6] C.-J. Yu, Advances in modelling and simulation of halide perovskites for solar cell applications, *Journal of Physics: Energy* **1**, 022001 (2019).
- [7] K. Sandeep, K. Padmakumar, K. U. Ambili, P. Jishnu, K. H. Fousia, A. R. Ramesh, J. P. Rappai, V. Santhi, and M. Shanthil, Anion exchange in lead halide perovskites: An overview, *physica status solidi (b)* **259**, 2100600.
- [8] N. Marzari and D. Vanderbilt, Maximally localized generalized wannier functions for composite energy bands, *Phys. Rev. B* **56**, 12847 (1997).
- [9] N. Marzari, A. A. Mostofi, J. R. Yates, I. Souza, and D. Vanderbilt, Maximally localized wannier functions: Theory and applications, *Rev. Mod. Phys.* **84**, 1419 (2012).
- [10] D. Gresch, Q. Wu, G. W. Winkler, R. Häuselmann, M. Troyer, and A. A. Soluyanov, Automated construction of symmetrized wannier-like tight-binding models from ab initio calculations, *Phys. Rev. Mater.* **2**, 103805 (2018).
- [11] T. I. Yusufaly, D. Vanderbilt, and S. Coh, Tight-binding formalism in the context of the pythtb package (2013).
- [12] G. Pizzi, D. Volja, B. Kozinsky, M. Fornari, and N. Marzari, Boltzmann: A code for the evaluation of thermoelectric and electronic transport properties with a maximally-localized wannier functions basis, *Computer Physics Communications* **185**, 422 (2014).
- [13] K. Momma and F. Izumi, *VESTA3* for three-dimensional visualization of crystal, volumetric and morphology data, *Journal of Applied Crystallography* **44**, 1272 (2011).
- [14] P. Giannozzi, S. Baroni, N. Bonini, M. Calandra, R. Car, C. Cavazzoni, D. Ceresoli, G. L. Chiarotti, M. Cococcioni, I. Dabo, A. D. Corso, S. de Gironcoli, S. Fabris, G. Fratesi, R. Gebauer, U. Gerstmann, C. Gougoussi, A. Kokalj, M. Lazzeri, L. Martin-Samos, N. Marzari, F. Mauri, R. Mazzarello, S. Paolini, A. Pasquarello, L. Paulatto, C. Sbraccia, S. Scandolo, G. Sclauzero, A. P. Seitsonen, A. Smogunov, P. Umari, and R. M. Wentzcovitch, Quantum espresso: a modular and open-source software project for quantum simulations of materials, *Journal of Physics: Condensed Matter* **21**, 395502 (19pp) (2009).

- [15] P. Giannozzi, O. Baseggio, P. Bonfà, D. Brunato, R. Car, I. Carnimeo, C. Cavazzoni, S. de Gironcoli, P. Delugas, F. Ferrari Ruffino, A. Ferretti, N. Marzari, I. Timrov, A. Urru, and S. Baroni, Quantum espresso toward the exascale, *The Journal of Chemical Physics* **152**, 154105 (2020), <https://doi.org/10.1063/5.0005082>.
- [16] A. A. Mostofi, J. R. Yates, G. Pizzi, Y.-S. Lee, I. Souza, D. Vanderbilt, and N. Marzari, An updated version of wannier90: A tool for obtaining maximally-localised wannier functions, *Computer Physics Communications* **185**, 2309 (2014).
- [17] S. Coh and D. Vanderbilt, Python tight binding (pythtb) (2022).
- [18] J. Kim, S.-C. Lee, S.-H. Lee, and K.-H. Hong, Importance of orbital interactions in determining electronic band structures of organo-lead iodide, *The Journal of Physical Chemistry C* **119**, 4627 (2015), <https://doi.org/10.1021/jp5126365>.
- [19] I. E. Castelli, J. M. García-Lastra, K. S. Thygesen, and K. W. Jacobsen, Bandgap calculations and trends of organometal halide perovskites, *APL Materials* **2** (2014).
- [20] G. Pizzi, D. Volja, B. Kozinsky, M. Fornari, and N. Marzari, Boltzmann: A code for the evaluation of thermoelectric and electronic transport properties with a maximally-localized wannier functions basis, *Computer Physics Communications* **185**, 422 (2014).
- [21] H. Jin, Y.-J. Zeng, J. A. Steele, M. B. J. Roeffaers, J. Hofkens, and E. Debroye, Phase stabilization of cesium lead iodide perovskites for use in efficient optoelectronic devices, *NPG Asia Materials* **16**, 24 (2024).
- [22] W. Kohn, A. D. Becke, and R. G. Parr, Density functional theory of electronic structure, *The Journal of Physical Chemistry* **100**, 12974 (1996), <https://doi.org/10.1021/jp960669l>.
- [23] T. I. Yusufaly, D. Vanderbilt, and S. Coh, Tight-binding formalism in the context of the pythtb package (2013).
- [24] Z. Wang, S. Ye, H. Wang, J. He, Q. Huang, and S. Chang, Machine learning method for tight-binding Hamiltonian parameterization from ab-initio band structure, *npj Computational Materials* **7**, 11 (2021).
- [25] R. S. Mulliken, A new electroaffinity scale; together with data on valence states and on valence ionization potentials and electron affinities, *The Journal of Chemical Physics* **2**, 782 (1934).

**SUPPLEMENTARY INFORMATION: DENSITY FUNCTIONAL LEVERAGED TIGHT-BINDING
INSIGHTS INTO INORGANIC HALIDE PEROVSKITES**

Misbah Shaheen and Sheharyar Pervez*
Faculty of Engineering Sciences
Ghulam Ishaq Khan Institute of Engineering Sciences and Technology

TABLE S1: Input parameters used in DFT calculations.

Material	Threshold (Ry)		k-mesh		Lattice constants (\AA)
	Ecut	Ecut-rho	SCF	NSCF	
CsPbBr ₃	80	144	$8 \times 8 \times 8$	$12 \times 12 \times 12$	$a, b, c = 5.995863$
CsPbBr ₂ I	40	160	$8 \times 8 \times 8$	$12 \times 12 \times 12$	$a, b = 5.994375, c = 6.763426$
CsPbBrI ₂	40	160	$8 \times 8 \times 8$	$12 \times 12 \times 12$	$a, b = 6.402284, c = 5.659454$
CsPbI ₃	40	240	$8 \times 8 \times 8$	$16 \times 16 \times 16$	$a, b, c = 6.219181$

Wannier Bands and orbitals

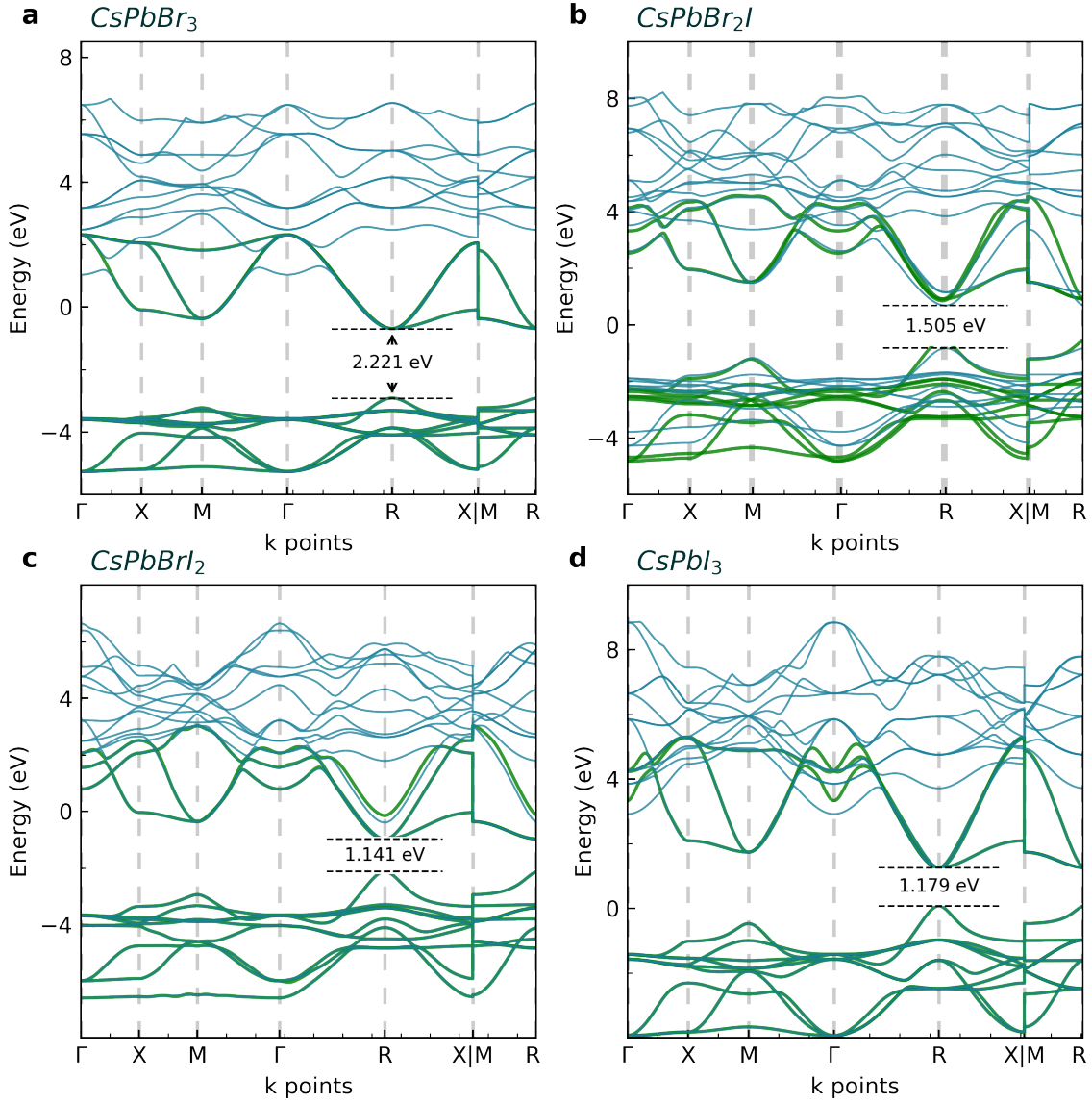


FIG. S1: Band structure obtained from Wannierization (green) and from DFT (blue). Twelve Wannier basis were selected for Pb and halogen p-orbitals for calculation.

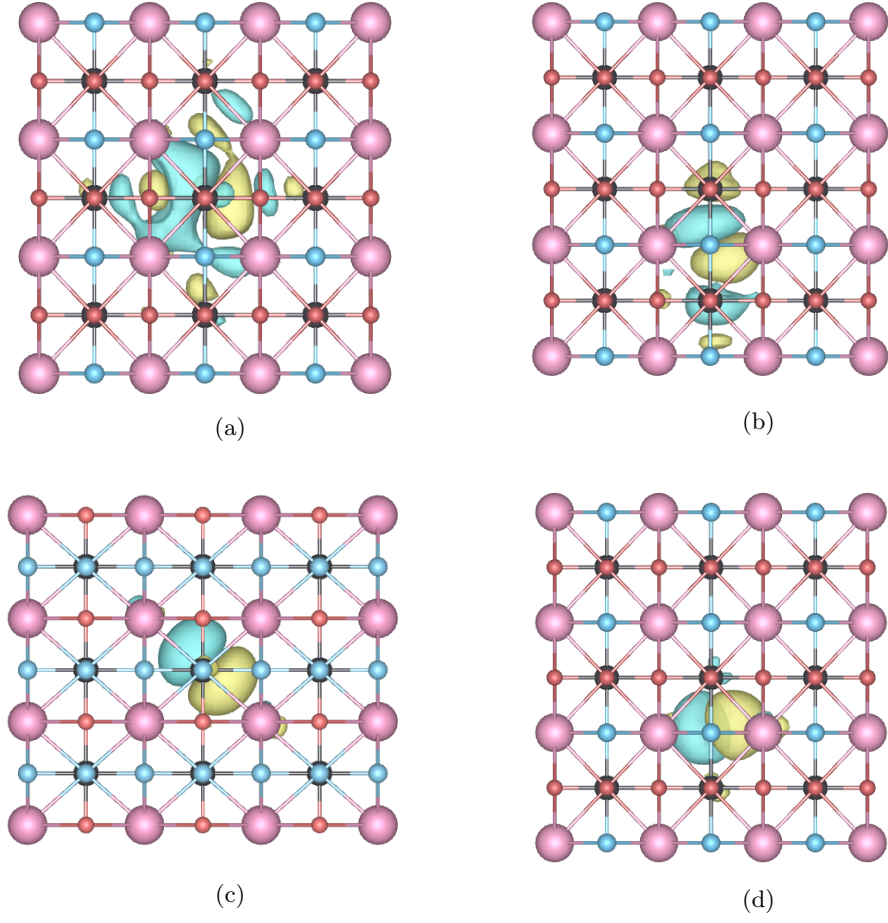


FIG. S2: Wannier orbitals (yellow and blue isosurfaces) of (a) Pb, (b-d) Halogen for anion exchanged CsPbBr_2I (Cs: pink, Pb: dark gray, Br: orange and I: blue) perovskite showing delocalized Pb and one of the halogen orbitals along with two relatively localized halogen orbitals.

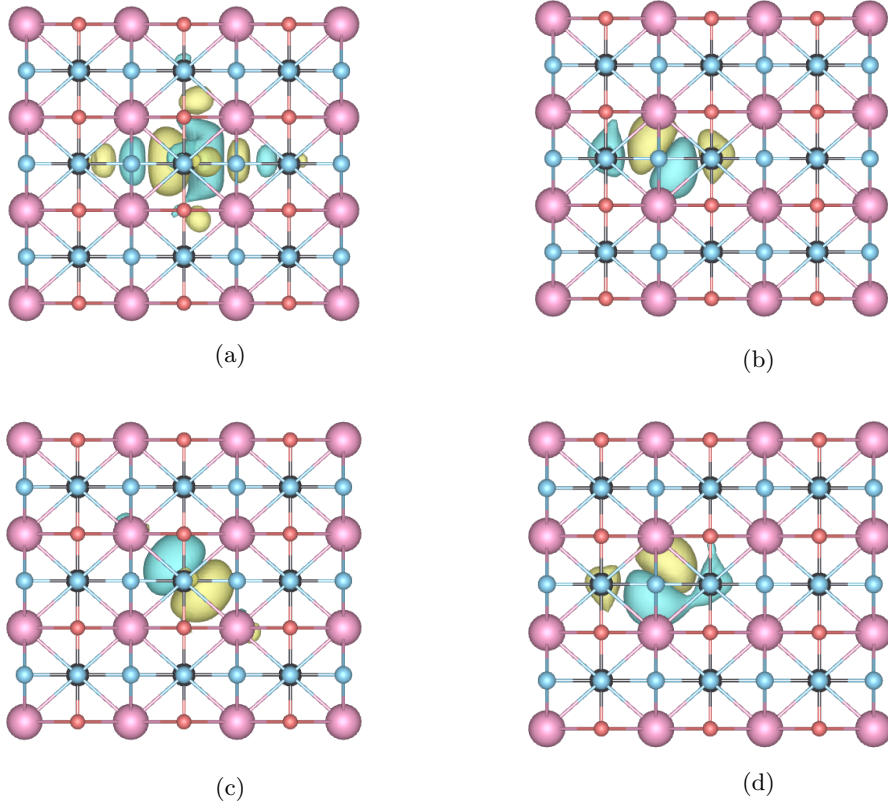


FIG. S3: Wannier orbitals (yellow and blue isosurfaces) of (a) Pb, (b-d) Halogen for anion exchanged CsPbBrI_2 (Cs: pink, Pb: dark gray, Br: orange and I: blue) perovskite showing delocalized Pb and one of the halogen orbitals along with two relatively localized halogen orbitals.

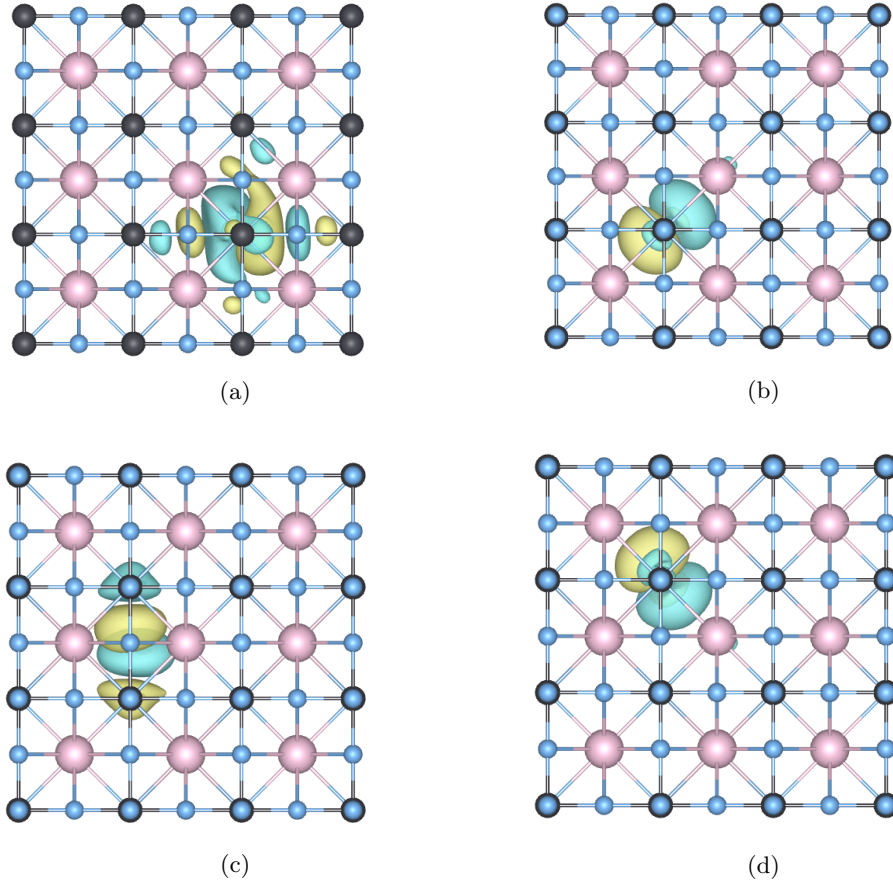


FIG. S4: Wannier orbitals (yellow and blue isosurfaces) of (a) Pb, (b-d) Halogen for anion exchanged CsPbI_3 (Cs: pink, Pb: dark gray, Br: orange and I: blue) perovskite showing delocalized Pb and one of the halogen orbitals along with two relatively localized halogen orbitals.

Reduced Tight Binding Scheme

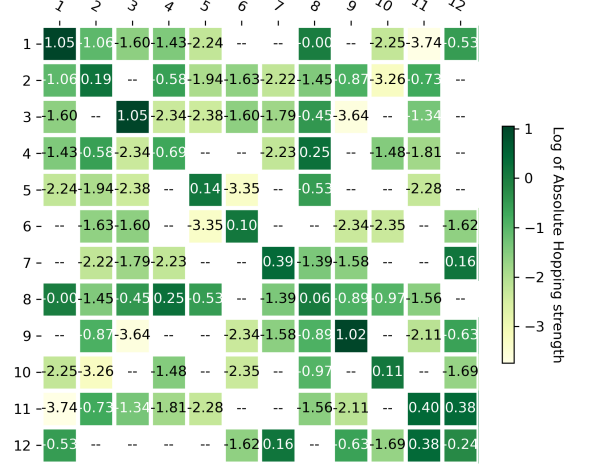
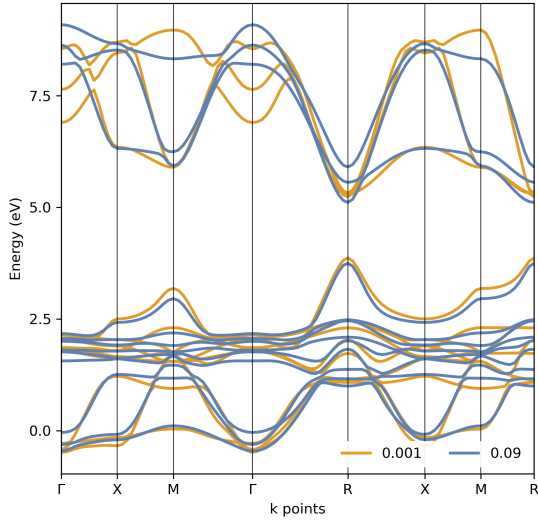
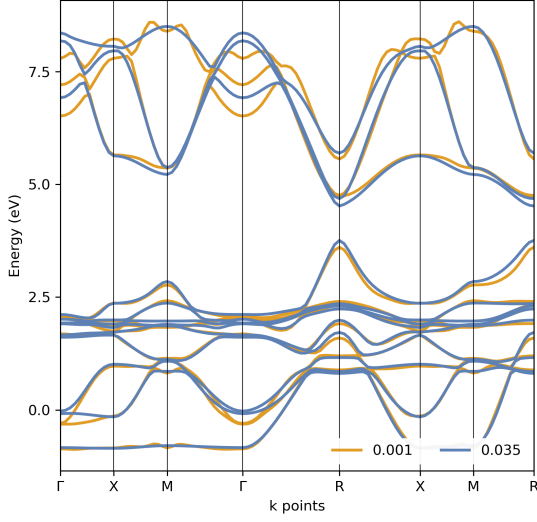
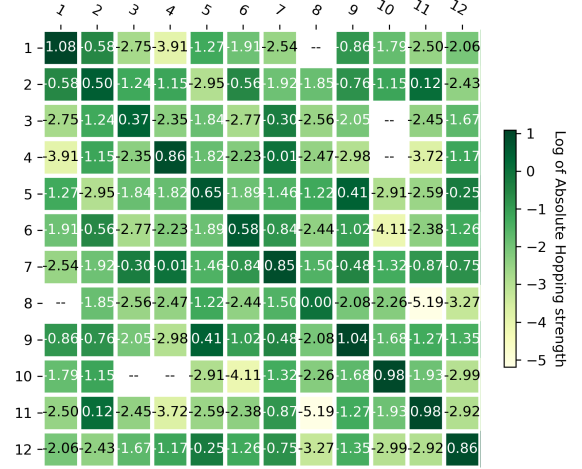


FIG. S5: (a) Band structure recovered using reduced tight binding scheme with minimum hopping norm of 0.09 (b) Heat map of reduced tight binding scheme for CsPbBr₂I .

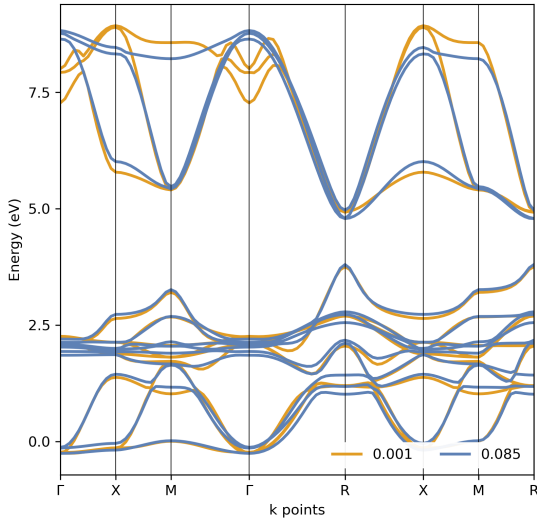


(a)

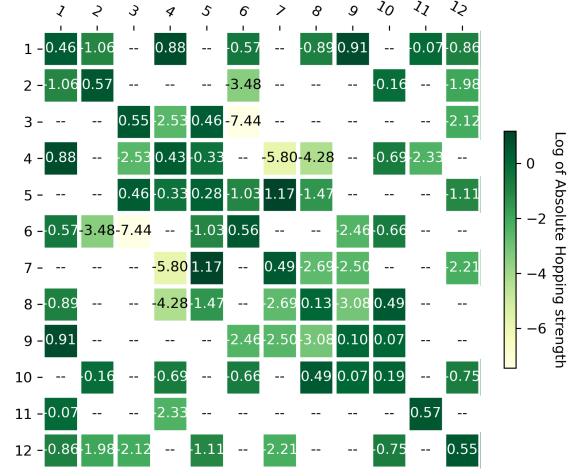


(b)

FIG. S6: (a) Band structure recovered using reduced tight binding scheme with minimum hopping norm of 0.035 (b) Heat map of reduced tight binding scheme for CsPbBr₂ .



(a)



(b)

FIG. S7: (a) Band structure recovered using reduced tight binding scheme with minimum hopping norm of 0.085 (b) Heat map of reduced tight binding scheme for CsPbI₃ .